

Strain-controlled electronic transport and exciton radiative lifetime in monolayer germanium sulfideVo Khuong Dien ^{1,*}, Pham Thi Bich Thao ², Nguyen Thi Han ³, Nguyen Duy Khanh ^{4,5}, Le Vo Phuong Thuan ⁶,
Ming-Fa Lin,⁶ and Nguyen Thanh Tien ^{2,†}¹*Department of Electrophysics, National Yang Ming Chiao Tung University, Hsinchu 300, Taiwan*²*College of Natural Sciences, Can Tho University, 3-2 Road, Can Tho City 94000, Vietnam*³*Faculty of Materials Science and Engineering, Phenikaa University, Hanoi 12116, Vietnam*⁴*Laboratory for Computational Physics, Institute for Computational Science and Artificial Intelligence, Van Lang University, Ho Chi Minh City, Vietnam*⁵*Faculty of Mechanical - Electrical and Computer Engineering, School of Technology, Van Lang University, Ho Chi Minh City, Vietnam*⁶*Department of Physics, National Cheng Kung University, 701 Tainan, Taiwan* (Received 26 June 2023; revised 7 September 2023; accepted 18 October 2023; published 6 November 2023)

Monolayer germanium sulfide (GeS) has gained significant attention for its exceptional anisotropic electronic conductance, notable excitonic effects, and wide range of applications. In this study we used density functional theory, the nonequilibrium Green's function, and many-body perturbation theory to investigate electronic transport properties and exciton radiative lifetime of single-layer germanium sulfide. Our theoretical findings showed that applying up to 8% compressive strain yielded a nearly threefold increase in carrier mobility and dramatically enhanced device's current intensity. Moreover, we observed that strain engineering allowed for fine-tuning of the electron-hole recombination time. At 6% tensile strain, the effective radiative lifetime was as short as 0.81 ps, which is 4 times faster than the intrinsic case and 24 times faster than at 8% compressive strain. These results highlight the potential of strain engineering to customize the electronic and optical properties of GeS monolayer for specific electronic, optoelectronic, and photovoltaic applications.

DOI: [10.1103/PhysRevB.108.205406](https://doi.org/10.1103/PhysRevB.108.205406)**I. INTRODUCTION**

The successful fabrication of monolayer graphene [1] has sparked significant interest in exploring other two-dimensional (2D) materials, including hexagonal boron nitride (h-BN) [2,3], transition-metal dichalcogenides (TMDCs) [4], group-III monochalcogenides [5,6], phosphorene [7], and others. Recently, 2D germanium sulfide (GeS) has emerged as a highly researched material [8–10]. Bulk GeS also adopts a layered structure like phosphorus, with weak van der Waals (vdWs) interactions between interlayers and strong covalent bonding within layers. The few layers of GeS have been successfully fabricated via either a vapor transport process [9] or mechanical exfoliation [10], while the monolayer GeS is predicted to be dynamically stable [11], suggesting the high ability to exfoliate the monolayer GeS from its bulk counterpart. Contrary to semimetal graphene, monolayer GeS possesses a sizable electronic band gap (~ 2.3 eV) [11], making it well suited for semiconductor applications. Additionally, the monolayer form of GeS is predicted to have a much larger free carrier mobility ($\sim 10^3$ cm² V⁻¹ s⁻¹) [11] compared to MoS₂ (~ 200 cm² V⁻¹ s⁻¹) [12]. As a result of the ultrathin monolayer and the significant reduction of dielectric screening, the excitonic effects are predicted to be very

strong in the GeS single layer [13,14]. One notable feature of GeS is its anisotropic electric conductance and optical responses [15], which distinguish it from isotropic 2D crystals such as graphene and MoS₂. Therefore, exploring ways to manipulate these anisotropies further would be exciting.

The current research focus on condensed-matter physics involves modifying the electronic and optical characteristics of layered materials [16,17]. This can be achieved through various methods such as introducing adatoms [18,19], applying electric and magnetic fields [20], adsorbing molecule clusters [16], and creating defects [21,22]. Another effective method for altering the properties of materials is strain engineering, which is particularly useful for one-dimensional [23] and two-dimensional [24] crystals due to their ability to withstand much larger strains compared to bulk crystals. For instance, monolayer MoS₂ [25] and graphene [26] can sustain strain up to their intrinsic limit (approximately 11% for MoS₂ and 15% for graphene) without causing significant damage to their crystal structures. This provides a wide range of opportunities for tuning their electronic optical properties.

Herein, by combining density functional theory (DFT) [27], the nonequilibrium Green's Function (NEGF) [28], and the many-body perturbation theory (MBPT) [29], we illustrate that strain engineering can serve as an effective tool to tailor the electronic transport properties and the recombination timescale of exciton states. Our theoretical calculations indicated that electron mobility could be significantly enhanced under compressive strain, and the I-V characteristic of the

*vokhuongdien@nycu.edu.tw

†nttien@ctu.edu.vn

device shows extremely high current intensity. Moreover, the excitonic effects, especially the radiative lifetime of excitons, can be fine-tuned upon applying the external strains. The theoretical results achieved in the current research are of paramount importance, not only for basic sciences but also for high-tech applications, such as ultrafast field-effect transistors (FETs), light-emitting diodes (LEDs), and photovoltaic (PV) applications.

II. COMPUTATIONAL DETAILS

In this study we utilized the Vienna Ab-initio Simulation Package (VASP) [30] to perform the ground-state and excited-state calculations of the biaxial strain GeS monolayer. For analyzing the electronic transport properties of the GeS monolayer, we employed QUANTUMATK simulation [31]. The exchange-correlation function was determined using the Perdew-Burke-Ernzerhof (PBE) generalized gradient approximation [32]. Additionally, the electronic wave functions in the core region were described using the projector-augmented wave (PAW) pseudopotentials [33]. A plane-wave basis expansion with a cutoff energy of 500 eV was chosen. The vacuum level was kept at 14 Å to avoid the interaction of the GeS layer with its periodic images. Geometric optimization utilized Monkhorst-Pack sampling [34] with a $32 \times 24 \times 1$ k -point mesh. The relaxation of all atoms was allowed until the Hellmann-Feynman force acting on each atom was smaller than 0.01 eV/Å.

On the top of Kohn-Sham wave functions, the single-shot GW (G0W0) approach [35] was employed for quasidelectronic-band-structure calculations. To ensure the accuracy of our calculation, we have performed convergence tests using various k -mesh values, and cut-off energy for the response functions, as well as the number of empty conduction bands. Our results (Fig. S2 in Supplemental Material [36]) demonstrated that the electronic properties are very sensitive to the input parameters, the k points of $36 \times 27 \times 1$, response functions with a cutoff energy of 120 eV, and 120 empty conduction bands were sufficient to achieve convergence for the quasiparticle band gap.

To investigate the optical response and excitonic effects, we solved the Bethe-Salpeter equation (BSE) [37] on top of the G0W0 calculations. The calculation considered six highest occupied valence bands and four lowest unoccupied conduction bands as a basis for the excitonic states, which covered a photon energy range of 0–5 eV.

III. RESULTS AND DISCUSSIONS

A. Electronic transport properties

As a typical benchmark to investigate the impact of strain effects on electronic and optical properties, we consider the geometric structure of pristine GeS monolayer, which is depicted in Fig. 1(a) and summarized in Table I. Similar to the phosphorene, monolayer GeS also exhibited a buckled structure with each germanium atom covalently bonded with three adjacent sulfur atoms. The optimized lattice constants are $a = 3.665$ Å (zigzag direction), and $b = 4.471$ Å (armchair direction). The calculated parameters are in good agreement

TABLE I. The optimized geometric parameters and the electronic band gap of monolayer germanium sulfide. The previous values of theoretical predictions and experimental measurements are also shown for comparison.

| a (Å) | b (Å) | Fundamental band gap (eV) | |
|--------------------|--------------------|---------------------------|--------------------|
| | | DFT | G0W0 |
| 4.471 ^a | 3.665 ^a | 1.728 ^a | 2.661 ^a |
| 4.470 ^b | 3.666 ^b | – | 2.74 ^b |
| 4.459 ^c | 3.662 ^c | 1.90 ^c | – |
| 4.33 ^d | 3.67 ^d | – | – |
| 4.492 ^e | 3.62 ^e | 1.713 ^e | – |
| 4.467 ^f | 3.666 ^f | 1.722 ^f | – |
| 4.474 ^g | 3.675 ^g | 1.82 ^g | – |
| 4.29 ^h | 3.64 ^h | – | – |

^aTheoretical data in this work.

^bTheoretical data in Ref. [15].

^cTheoretical data in Ref. [38].

^dTheoretical data in Ref. [11].

^eTheoretical data in Ref. [39].

^fTheoretical data in Ref. [40].

^gTheoretical data in Ref. [41].

^hExperimental data for GeS bulk in Ref. [42].

with previous theoretical calculations [38–41] and quite close to the experimental measurements of GeS bulk [42].

The electronic band structure along the high-symmetry points within DFT and G0W0 levels of theory is shown in Fig. 1(b). Since the spin-orbit coupling (SOC) influences only marginally on the electronic band gap of GeS (Fig. S3 [36]), the relativistic effects are ignored in our calculations for the sake of reducing the computational cost. GeS exhibits anisotropic electronic properties; the dispersion of the occupied hole along the $\Gamma - Y$ direction is significant, indicating the small effective mass. The opposite behavior is true for hole transport along the $\Gamma - X$ direction with relatively flat energy dispersion related to the large effective mass. Similar characteristics are also found for the electron in the unoccupied states. The anisotropy of these bands can be easily detected by the 3D contour plot in Fig. 1(c), while the spatial dependent of electron and hole effective mass of the GeS monolayer, which exhibits the “heart” and “peanut” shapes, are illustrated in Fig. S4 (see Supplemental Material [36]). The GeS monolayer is an indirect band gap of 1.735 eV with the highest occupied state and lowest unoccupied state located between Γ and Y and Γ and X symmetry points, respectively. It is well known that the PBE functional underestimates the band gap of semiconductors, and while the GW calculation gives an adequate value [44], the electronic band gap is enhanced to 2.661 eV when the electron-electron interactions (GW approximations) are adopted. The theoretical prediction is in good agreement with previous works (Table I).

Figure 1(d) depicts the electronic properties of a strained GeS monolayer, with critical points A, B, C, D, and E marked by red dots indicating the band-edge states that make the band-gap evolution. The corresponding orbital characters for these critical points are shown in Fig. 1(e) and are organized into five categories: (A) out-of-plane interactions of Ge- $4p_z$ and S- $3p_z$ orbitals, (B) out-of-plane hybridizations of Ge- $4p_z$

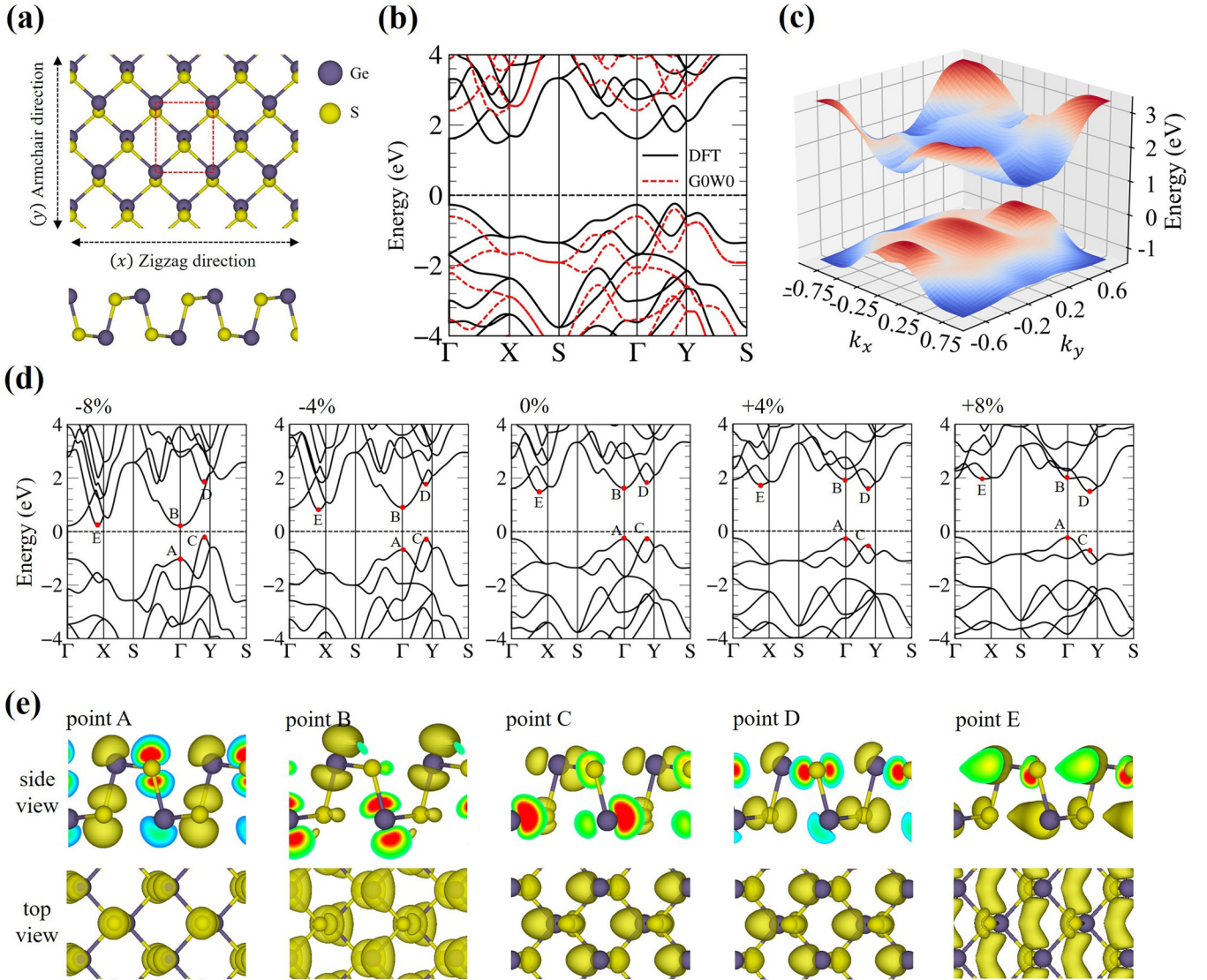


FIG. 1. Geometric and electronic characteristics of pristine and strained GeS monolayer. (a) Geometric structure of single-layer GeS shown in top and side views. The red dashed rectangle illustrates the unit cell used in the calculation. (b) Electronic band structure of GeS monolayer depicted using DFT and G0W0 levels of theory. (c) Three-dimensional (3D) band structure of GeS monolayer. (d) Variation of electronic band structure of strained GeS monolayer using DFT. (e) Band-decomposed charge density at critical points marked by red dots in (d). The G0W0 quasiparticle band structure of GeS monolayer in this work was achieved under WANNI90 codes [43].

and S- $(3p_x, 3p_y)$ orbitals, (C) in-plane couplings of Ge- $4p_y$ and S- $3s$ orbitals, (D) interactions of in-plane Ge- $4s$ and S- $3p_y$ orbitals, and (E) in-plane interactions of Ge- $4p_x$ and S- $3p_x$ orbitals. As indicated in Fig. S5 and Table S1 [36], compressive strain causes the d_2 chemical bonding and h vertical height to increase, significantly reducing the out-of-plane Ge- $4p_z$ and S- $3p_z$ orbital interactions, as well as the Ge- $4p_z$ and S- $(3p_x, 3p_y)$ orbital interactions. This reduction leads to a significant downward shift in energy levels for the edge states at A and B. On the other hand, the interactions of in-plane couplings of Ge- $4p_y$ and S- $3s$, and Ge- $4s$ and S- $3p_y$ orbitals increase due to the d_1 chemical bonding reduction, resulting in an increase in energy for the edge states C and D. A decrease in the α angle reduces in-plane interactions of Ge- $4p_x$ and S- $3p_x$ orbitals, causing a downshift in the energy of the E critical point. Conversely, the opposite evolution takes place

for tensile strains, d_2 chemical bonding, and h vertical height decrease, raising energy levels for edge states A and B, while d_1 chemical bonding elongates, decreasing energy levels for edge states C and D. The critical point E moves upward as a consequence of increasing the α angle.

Figure S5(d) [36] displays the evolution of the band gap for the strained GeS monolayer. The electronic band gap decreases linearly with increasing compressive pressure. However, the band-gap evolution under tensile strain is more complex. The electronic band gap initially increases to 1.9 eV, accompanied by an indirect-direct transition. However, at higher tensile strains, the gap value dramatically decreases, and the same trend is observed in the band-gap evolution with the GW corrections.

To connect the anisotropic band dispersion with the electronic conductance, we further estimated the carrier mobility

along the zigzag and armchair directions according to the deformation theory [45,46]:

$$\mu_{2D} = \frac{e\hbar^3 C_{2D}^i}{k_B T m_i^* m_d E^{i2}}. \quad (1)$$

In this context, the symbol m_i^* represents the effective mass in the direction of transport, while $m_d = \sqrt{(m_x^* m_y^*)}$ represents the average effective mass. The elastic module C_{2D}^i can be determined by fitting the quadratic relationship between the total energy E and the variation in lattice constant $\delta l/l_0$, expressed as $(C_{2D}/2)(\delta l/l_0)^2 = (E - E_0)/S_0$. Here, S_0 denotes the equilibrium lattice area of the 2D lattice. The deformation-potential constant $E^i = \partial E_{edge} \partial \epsilon$ is obtained by examining the changes in the valence-band maximum (VBM) or conduction-band minimum (CBM) due to slight lattice compression or expansion along the transport direction. The theoretical analysis is conducted at a room temperature of $T = 300$ K. It is important to note that this estimation only provides a simple representation of electron-phonon interactions and may consequently overestimate the actual carrier mobility. Nevertheless, this prediction is sufficiently accurate to capture the anisotropic behavior of conductance and its tendency under strains.

Since the effective mass of carriers in the zigzag and armchair directions behaves differently and exhibits two extreme values (Fig. S4 [36]), we focus on calculating the effective mass and mobility for carriers along the $\Gamma - X$ and $\Gamma - Y$ paths. Figure 2(a) illustrates the strain-dependent effective mass of the highest valence hole and lowest conduction electron, which demonstrates a linear decrease under compressive strain. This decrease reflects the band curvature shown in Fig. 1(d) and contributes to enhanced carrier mobility. The carrier effective mass increases significantly under an elongation of the lattice constant, and the anisotropy of carriers along the calculated directions becomes more pronounced. Additionally, the evolution of effective mass is complex. For example, there is a notable jump in m_h^* (zigzag) at 2% tensile strain due to the transition of the VBM from $\Gamma - Y$ to Γ band-edge states, resulting in a shift from light holes to heavy holes.

The calculated carrier mobility of the GeS monolayer at room temperature ($T = 300$ K) according to the compression and elongation of the lattice constant is shown in Fig. 2(b). In the intrinsic case, the relatively small effective mass of electrons and the significant C_{2D}^i/E^{i2} ratio (Table S2 [36]) contribute to the high electron carrier mobility of the GeS monolayer, with a typical value of $13 \times 10^3 \text{ cm}^2 \text{ V}^{-1} \text{ s}^{-1}$ for electrons in the zigzag direction and about $0.35 \times 10^3 \text{ cm}^2 \text{ V}^{-1} \text{ s}^{-1}$ for electrons in the armchair direction. The carrier mobility values for valence holes are lower, with about $0.061 \times 10^3 \text{ cm}^2 \text{ V}^{-1} \text{ s}^{-1}$ and $0.036 \times 10^3 \text{ cm}^2 \text{ V}^{-1} \text{ s}^{-1}$ for zigzag and armchair directions, respectively. The high electron mobility of 2D GeS is consistent with previous reports [11,47] and compatible with that of phosphorene [48], but much higher than that of MoS₂ [4], indicating its potential for high-speed electronic applications. As expected, carrier mobility decreases upon lattice expansion due to the increasing carrier effective mass and the decreasing of C_{2D}^i/E^{i2} ratio. This evolution is similar to that observed

in Ref. [49]. Conversely, the mobility of carriers significantly increases with lattice compression. Although the mobility of holes can be controlled by applying external strain, it cannot surpass that of the electrons. Interestingly, under 8% of compression, the mobility of electrons along a zigzag direction reaches approximately $35 \times 10^3 \text{ cm}^2 \text{ V}^{-1} \text{ s}^{-1}$, more than 2.5 times and 400 times larger than the values under free strain and 8% tensile strain, respectively.

Due to its exceptionally high carrier mobility, we opted for strained GeS monolayers as the channel material in our device construction. The transport properties have been calculated via the NEGF method as implemented in the QUANTUMATK package [31]. $50 \times 50 \times 1$ k points were used for the central region and the electrodes. When a given voltage is applied, the current is allowed to flow across the system. The electric current (I) is further calculated using the Landauer approach [50], and this can be obtained from the integration of the transmission curve as

$$I(V_b) = \frac{2e}{h} \int_{-\infty}^{+\infty} T(E, V_b) [f(E - \mu_L) - f(E - \mu_R)] dE, \quad (2)$$

where $f(E - \mu_{L/R})$ is the Fermi-Dirac distribution function of the left (L) and right (R) electrodes, $\mu_{L/R}$ is the chemical potential, and $T(E, V_b)$ is the transmission function at energy E and bias voltage V_b . The expression of $T(E, V_b)$ is as follows:

$$T(E, V_b) = \text{Tr}[\Gamma_L(E, V_b) G(E, V_b) \Gamma_R(E, V_b) G^\dagger(E, V_b)], \quad (3)$$

in which the coupling matrices are given as $\Gamma_{L/R}$, and the retarded and the advanced Green's functions of the scattering region are presented as G^\dagger and G .

Figures 2(e) and 2(f) illustrate the fundamental architecture of the GeS device, highlighting its transport characteristics along the zigzag and armchair directions. These properties are further depicted in Figs. 2(c) and 2(d). Given the negligible carrier mobility of holes, our primary focus lies on the transport properties of electrons. To achieve efficient carrier injection and attain optimal device performance, we employ left and right electrodes with an n -type doping concentration of $4.8 \times 10^{12} \text{ e/cm}^2$. The intrinsic monolayer GeS exhibits a remarkable anisotropic behavior in its transport properties. The $I - V$ curve, when biased along the zigzag direction, resembles that of a characteristic semiconductor, with a peak current of approximately 1200 nA at $V_{\text{bias}} = 2$ V. Conversely, carrier transport along the armchair direction is negligible, with the highest current reaching only 0.012 nA at 0.2 V, followed by slight fluctuations at higher applied voltages. These anisotropic transport characteristics of the intrinsic GeS monolayer align well with previous findings [51] and reflect the primary trend in carrier mobility in their respective directions. Both models demonstrate a high sensitivity of the $I - V$ curves to external strain. As the lattice elongation increases, the maximum current intensity of the zigzag and armchair models experiences a sharp decline. Both models exhibit strong negative differential resistance, indicating a diminishing of current intensity with increasing bias voltage, particularly evident under 8% lattice elongation. Interestingly, the $I - V$ curves of the GeS monolayer device under compression consistently exhibit semiconductor characteristics. The current intensity of the compressive GeS device experiences

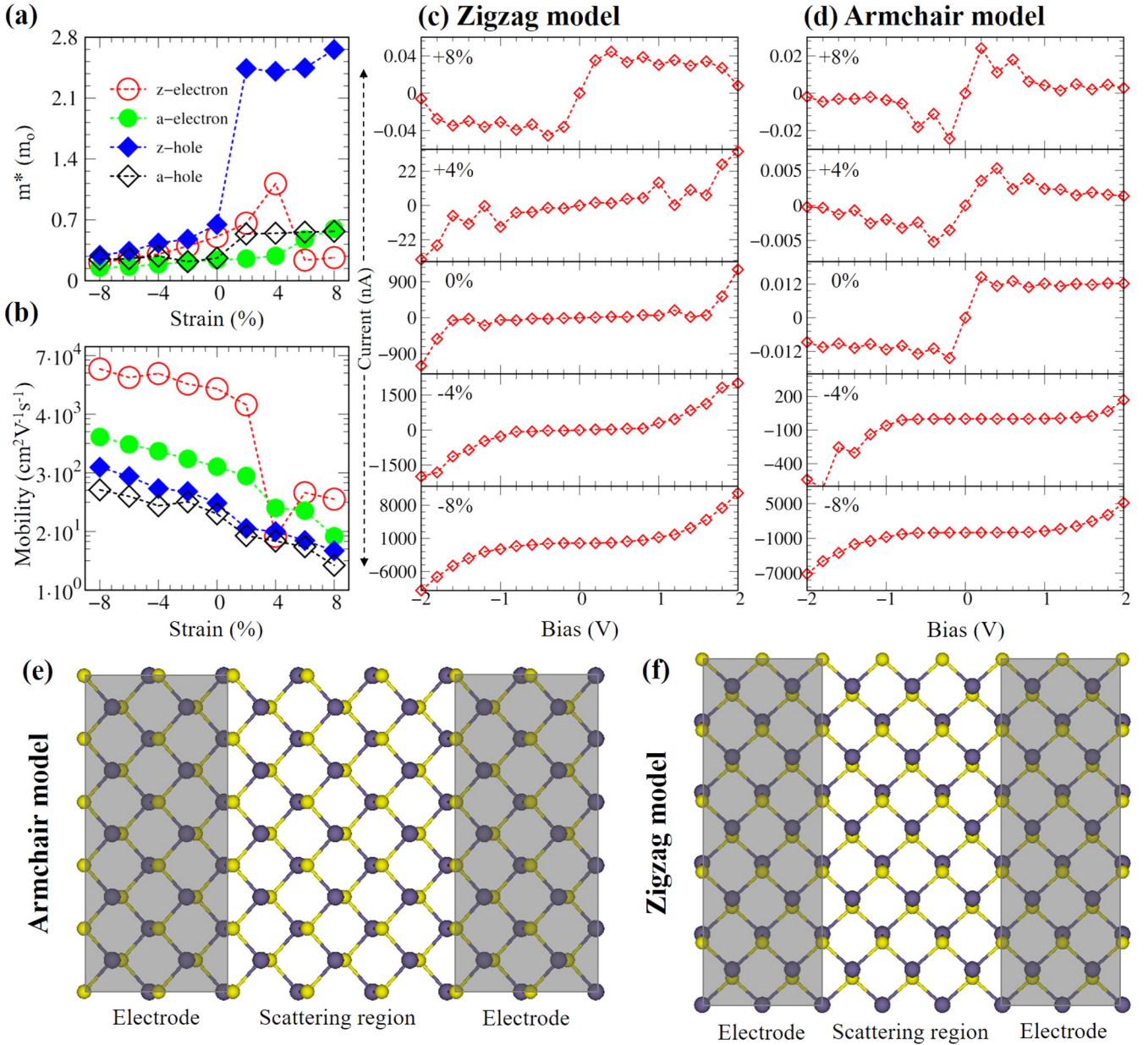


FIG. 2. Transport characteristics of strained GeS monolayer. (a) Evolution of effective mass and (b) carrier mobility under biaxial strains. (c) I-V characteristics for electron transport along the zigzag direction at different biaxial strains. (d) I-V characteristics for electron transport along the armchair direction at different biaxial strains. Device models for electron transport along (e) the armchair direction (armchair model) and (f) the zigzag direction (zigzag model) in strained GeS monolayer. The electrode and the active regions were constructed using two- and three-unit cells, respectively.

a significant enhancement. For the zigzag model, the highest current intensity exceeds 2000 nA and 10 000 nA under 4% and 8% compression, respectively, whereas the corresponding values for the armchair model are approximately 170 and 5200 nA, respectively. These findings indicate that the devices of compressively strained GeS monolayers possess an extremely high sensitivity, making them well suited for high-speed electronic applications.

B. Optical properties and excitonic effects

To obtain an accurate exciton spectrum, it is crucial to consider the convergence properties of the Bethe-Salpeter

equation. Figure S2(d) [36] demonstrates that the positions of the exciton states, particularly those at higher energies, exhibit remarkable sensitivity to the number of k points employed in the BSE calculation. As the number of k points increases, the energy of the exciton states progressively rises until convergence is achieved at approximately 1000 k mesh.

Figure 3 shows the optical properties of the GeS monolayer with and without excitonic effects. The absorbance spectra exhibit significant anisotropy due to the nonuniform environment along the armchair and zigzag directions. The low-frequency optical properties are primarily influenced by the armchair polarization. The selection rules for anisotropic optical response is further discussed in the Supplemental

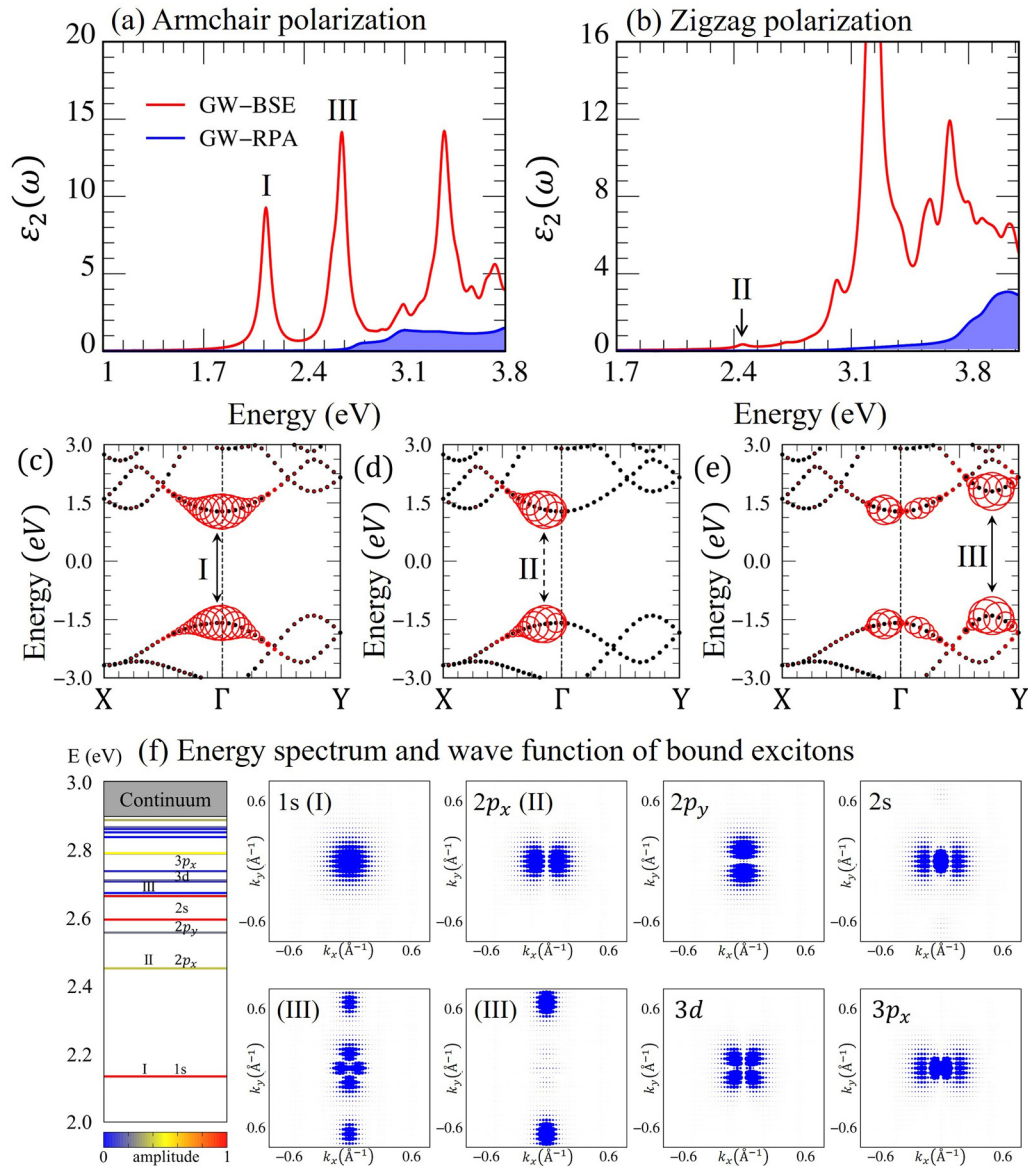


FIG. 3. The imaginary part of dielectric functions $\epsilon_2(\omega)$ for intrinsic GeS monolayer with polarization along the (a) armchair and (b) zigzag directions. The imaginary part of dielectric functions, including excitonic effects, is represented by the red curve, while the blue-filled curve excludes these effects. Exciton wave functions, projected onto the electronic band structure, are shown for (c) I, (d) II, and (e) III excitons, demonstrating vertical excitation from the valence-band maximum (VBM) to the conduction-band minimum (CBM). The radii of circles indicate the contribution of electron-hole pairs at specific k points to the respective exciton wave function, with the background dots representing the corresponding G0W0 quasiparticle band structures. (f) The exciton energy spectrum of the pristine GeS monolayer and the k -space distribution of the envelope functions for the first eight excitons. Excitonic amplitudes (color scale in the left panel) are normalized with respect to the brightest exciton among all the exciton states from blue (optically dark exciton) to red (bright exciton). The exciton states (right panels) are labeled with primary and azimuthal quantum numbers according to their nodal structure in the radial and azimuthal directions, respectively. The III exciton states were excluded from the hydrogenlike model due to their association with electron-hole pairs originating from different valleys.

Material [36]. In the absence of strain, the optical properties of GeS along the armchair and zigzag directions are characterized by three exciton states, denoted as I, III, and II in Figs. 3(a) and 3(b), respectively. The first two excitonic states are a result of the interaction between excited holes and electrons at the Γ valley, while the third state originates from carriers at the critical point along the $\Gamma - X$ direction, as depicted by the fat band in Figs. 3(c)–3(e). The intensity of the II exciton state is rather weak. In contrast, the

opposite behavior, characterized by high dipole matrix amplitudes, is true for the I and III excitons. The weak intensity of the II exciton state can be partially attributed to its greater quantum number. When excitons possess higher quantum states, they typically spread over a larger area within the material [52]. This expanded spatial separation between the electron and hole results in a reduction in the overlap of their wave functions, ultimately leading to diminished transition dipole moments. To assess the strength of excitonic effects,

we calculated exciton binding energy as the energy difference between the optical gap and the fundamental direct GW band gap at Γ . The exciton binding energy of the GeS monolayer is about 0.706 eV (Table S4 [36]) and is consistent with previous reports [13]. The large binding energies and the significant modifications in the absorption spectra (compared with GW-RPA spectra) indicate that these exciton states are strong and potentially stable at high temperatures. The dissociation temperature T_d ($T_d \simeq 0.1E_b/K_B$) for the I exciton is around 800 K, which is much higher than room temperature.

To better understand the character of specific exciton states, Fig. 3(f) illustrates the energy diagram of the bound exciton states in the GeS monolayer, as well as the k -space distribution of the squared amplitude of the exciton wave functions in the Brillouin zone. In addition to the bright exciton states with high transition probabilities, the presence of significant low optical transition dipole moments also gives rise to numerous dark exciton states, which are manifested by blue-gray colors in Fig. 3(f). Although not detectable in the optical absorbance spectra, the dark exciton states are important, as they provide fingerprints for the optical properties of typical materials. The nodal structures of these excitonic wave functions reveal a hydrogenlike series of states with clear angular momentum assignments. Interestingly, the excitonic energy diagram does not follow the Rydberg series for the 2D hydrogenic model, in which excitons with higher azimuthal quantum numbers have lower energies than those with smaller azimuthal quantum numbers. For instance, the energy of $2p_x$ and $2p_y$ excitons is smaller than that of the $2s$ ones, and this behavior is universal in 2D materials due to their unique screening [52,53]. Another noteworthy feature is the degeneracy of the $2p$ states resulting from the in-plane anisotropy, which is a characteristic of the GeS monolayer and other 2D materials [54,55].

Figure 4(a) illustrates the optical excitation of GeS when subjected to biaxial strain, while Fig. 4(b) summarizes the changes in the optical gap, the direct valence-to-conduction band transition energy, and the exciton binding energy. For the sake of simplification, we focus only on the features of the first bright I exciton. When compressed, the optical gap decreases due to the reduction of the corresponding direct electronic band gap. The exciton binding energy of prominent excitations and their intensity exhibits a significant alteration. The most notable feature is that the exciton binding energy of GeS under compressive strain is weaker than that of the strain-free and lattice-expanded cases. This is primarily due to the enhanced screening ability (increase in static dielectric constant $\epsilon_1(0)$, as shown in Table S3 [36]) or the reduction of the electronic band gap. Additionally, the anisotropy of the optical spectrum along the armchair and zigzag polarizations at 6% compressive strain gradually decreases compared to that of the intrinsic case, but they start to distinguish at the higher applied strain. This is due to the evolution of the electronic anisotropy of the GeS monolayer under compression, as indicated by the contour plots of the direct valence-to-conduction band transitions in Fig. 5.

Conversely, when subjected to lattice expansion, the optical gap increases, and the exciton binding energy as well as the anisotropy of the optical spectrum exhibit opposite changes to those observed under compression. The changes in optical properties of the GeS monolayer upon elongation are rather

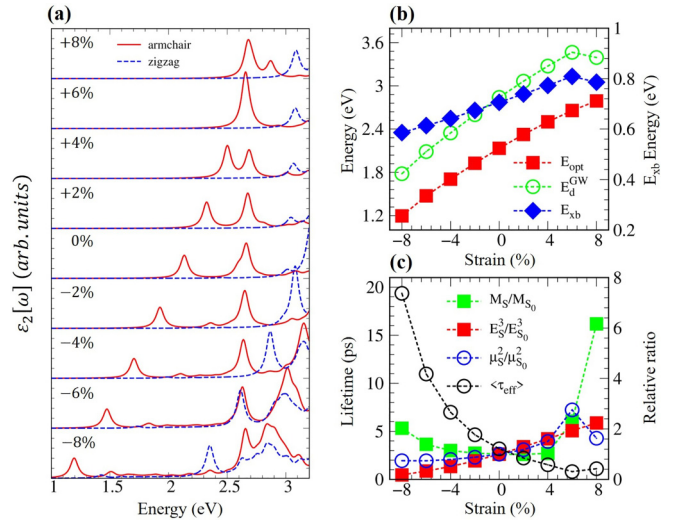


FIG. 4. Strain-dependent optical properties of a GeS monolayer. (a) Variation of the imaginary part of the dielectric function [$\epsilon_2(\omega)$] with external strains applied to the GeS monolayer. (b) Evolution of strain-induced changes in the energy of the first exciton state and/or optical gap (E_{opt}), the direct valence-to-conduction band transition energy (E_d^{GW}) corresponding to the first bright exciton state, and the exciton binding energy (E_{xb}). (c) Dependence of the effective radiative lifetime (τ_{eff}), the exciton effective mass ratio (M_S/M_{S_0}), the oscillation strength ratio ($\mu_S^2/\mu_{S_0}^2$), and the energy ratio ($E_S^3/E_{S_0}^3$) of the first bright exciton state on external strain.

complicated, as the optical gap gradually increases but then slowly decreases at higher applied strain. The anisotropy of optical properties along the armchair and zigzag directions becomes more pronounced due to the nonuniform electronic wave functions of the tensile-strained GeS monolayer (Fig. 5). Moreover, the exciton binding energy and the intensity of the first bright I exciton state significantly increase. The evolution of binding energy of the first bright exciton state could be deduced by the increase of the electronic band gap or decrease of the dielectric screening environment (Table S3 [36]). On the other hand, the enhancement of its intensity can be interpreted as follows: the excited hole mostly localized around the germanium atom, while the excited electron relied around the sulfur atom of the opposite plane, as shown in the two first panels of Fig. 1(d) and replotted in Fig. S6. The significant reduction of monolayer thickness of GeS upon lattice expansion induces the hole and electron to get closer, thereby enhancing the electron-hole overlap, and the transition probability, as well as exciton binding energy. However, the impact of electron-hole physical distance does not always express the linear relation, and the binding energy of excitons and their oscillation strength begin to decrease when the critical strain reaches +8%. This phenomenon occurs because the nature of the first bright state gradually shifts from the I exciton state to the III exciton state as the GeS monolayer undergoes elongation. This information is illustrated in Fig. 5.

Based on the above discussion, it was found that strain plays a vital role in modifying the recombination probability of excited states. Specifically, we conducted additional analysis on the radiative lifetimes of excitons in the GeS monolayer. It is worth noting that the short lifetime of excitons can be

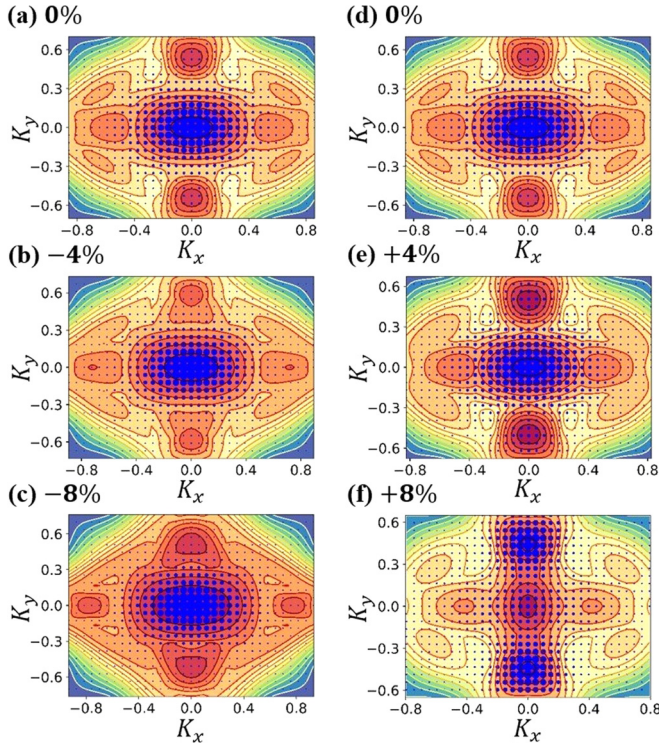


FIG. 5. Energy transition and exciton states in strained GeS monolayer. The color map represents the direct valence-to-conduction band transition energies within the first Brillouin zone of a strained GeS monolayer. The red area indicates the low-energy regime, while the green area illustrates the high-energy regime. The blue circles depict the wave functions of the first exciton state. Under compression of the 2D GeS lattice, the electronic functions become more isotropic, and the exciton state denoted as I corresponds to a 1s orbital. Conversely, an elongated lattice constant reveals noticeable differences in wave functions along the zigzag (K_x) and armchair (K_y) directions. The energies of I and III exciton states approach each other, and at an 8% elongation of the lattice constant, the III exciton state surpasses the I state, resulting in a switch in their nature.

advantageous for internal quantum efficiency and telecommunications applications. Conversely, the ultralong timescale of electron-hole recombination is highly beneficial for advanced optoelectronic and thin-film photovoltaic cells. Using the methodology developed for assessing radiative exciton lifetimes in 2D materials [56], the radiative lifetime $\langle \tau_S \rangle$ at room temperature ($T = 300$ K) of exciton states S is defined as follows:

$$\langle \tau_S \rangle = \left(\frac{8\pi e^2 E_S(0) \mu_S^2}{\hbar^2 c A_{uc}} \right)^{-1} \frac{3}{4} \left(\frac{E_S(0)^2}{2M_S c^2} \right)^{-1} k_B T, \quad (4)$$

where A_{uc} is the area of the unit cell, μ_S^2 is the square modulus of the BSE exciton transition dipole divided by the number of 2D k points, and $E_S(0)$ is the exciton energy calculated using the BSE method, and $M_S = m_e^* + m_h^*$ is the effective mass of the exciton. It is important to note that $m_{e(h)}^*$ here indicates the effective mass of the excited electron (hole) related to the exciton bound state but not for the effective mass of the CBM (VBM), as discussed in the electronic transport section. Although the model is simple and the effects of

momentum-forbidden and spin-forbidden dark excitons [57] does not directly account, it remains sufficiently accurate to predict the exciton lifetime for a variety of 2D materials, such as MoS₂ [58], GaN [59], and graphitic carbon nitride nanosheets [60]. Therefore it can be valuable in predicting the exciton lifetimes of strained GeS monolayers. At zero strain, the exciton lifetime of I, II, and III excitons is about 3.17 ps, 5.14 ns, and 0.79 ps. The ultralong lifetime of dark II excitons arises from its extremely small dipole strength.

With the assumed presence of perfect thermalization of the exciton states, we further define an effective radiative lifetime $\langle \tau_{\text{eff}} \rangle$ by averaging the decay rates over the lowest energy bright and dark excitons:

$$\langle \tau_{\text{eff}} \rangle^{-1} = \frac{\sum_S \langle \tau_S \rangle^{-1} e^{-E_S(0)/k_B T}}{\sum_S e^{-E_S(0)/k_B T}}. \quad (5)$$

The GeS monolayer exhibits an effective exciton lifetime of approximately 3.18 ps, which is close to that of I exciton and comparable to blue phosphorene (2 ps) [61], but faster than MoS₂ (0.83 ns) [58,62] and MoSe₂ (0.87 ns) [58].

Figure 4(c) illustrates the relationship between strain and the effective exciton lifetime. We also include the changes in relative effective mass (M_S/M_{S_0}), relative oscillation strength $(\mu_S/\mu_{S_0})^2$, and the energy ratio of the I exciton state $(E_S/E_{S_0})^3$ for comparison, as it significantly contributes to the effective exciton lifetime. In Fig. 4(c) it is evident that compressive strain causes a rapid increase in $\langle \tau_{\text{eff}} \rangle$ due to a decrease in oscillation strength and exciton energy, as well as an increase in effective mass. For instance, at 0% strain, the approximate value of $\langle \tau_{\text{eff}} \rangle$ is 3.18 ps. However, at -4% and -8% strains, the corresponding values of $\langle \tau_{\text{eff}} \rangle$ are approximately 6.99 ps and 19.36 ps, respectively. In contrast, although there is a significant enhancement in effective exciton mass, the radiative lifetime gradually decreases with applied tensile strain but starts to increase at +8% strain. This behavior is likely due to significant changes in the exciton transition dipole and an increase in the exciton energy. At 6% tensile strain, the smallest effective radiative lifetime is about 0.81 ps, which is 4 times faster than the intrinsic case and 24 times faster than the case with 8% compressive strain.

IV. CONCLUSIONS

To summarize, our study focused on examining the impact of biaxial strain on the electronic transport properties and exciton radiative lifetime of the GeS monolayer. The theoretical works are based on the combination of highly precise simulations and the appropriate theoretical models, such as DFT, MBPT, NEGF, the deformation-potential theory for carrier mobility, and the developed exciton lifetime for 2D materials. Our findings revealed a significant enhancement in the I-V characteristic when the lattice is compressed due to an improvement in carrier mobility. The optical gap, the anisotropic optical properties, the absorption coefficient, and the exciton binding energy strongly depend on the applied biaxial strain. Moreover, the strain also can finely adjust the timescale of electron-hole recombination. Compressive strain leads to a rapid increase in the effective recombination time $\langle \tau_{\text{eff}} \rangle$. Conversely, the radiative lifetime gradually decreases when tensile strain is applied. With the electronic and optical

properties that can be flexibly modified via strain engineering, the GeS monolayer may hold great potential for high-tech applications such as ultrafast FETs, PVs, and optoelectronic applications.

ACKNOWLEDGMENT

This research was funded by the Vietnam Ministry of Education and Training under Grant No. B2023-TCT-03.

- [1] A. K. Geim and K. S. Novoselov, *Nat. Mater.* **6**, 183 (2007).
- [2] J. D. Caldwell, I. Aharonovich, G. Cassabois, J. H. Edgar, B. Gil, and D. Basov, *Nat. Rev. Mater.* **4**, 552 (2019).
- [3] K. Zhang, Y. Feng, F. Wang, Z. Yang, and J. Wang, *J. Mater. Chem. C* **5**, 11992 (2017).
- [4] B. Radisavljevic, A. Radenovic, J. Brivio, V. Giacometti, and A. Kis, *Nat. Nanotechnol.* **6**, 147 (2011).
- [5] X. Li, J. Dong, J. C. Idrobo, A. A. Puzos, C. M. Rouleau, D. B. Geohegan, F. Ding, and K. Xiao, *J. Am. Chem. Soc.* **139**, 482 (2017).
- [6] T. Cao, Z. Li, and S. G. Louie, *Phys. Rev. Lett.* **114**, 236602 (2015).
- [7] A. Carvalho, M. Wang, X. Zhu, A. S. Rodin, H. Su, and A. H. Castro Neto, *Nat. Rev. Mater.* **1**, 16061 (2016).
- [8] E. Sutter, B. Zhang, M. Sun, and P. Sutter, *ACS Nano* **13**, 9352 (2019).
- [9] D. Tan, H. E. Lim, F. Wang, N. B. Mohamed, S. Mouri, W. Zhang, Y. Miyauchi, M. Ohfuchi, and K. Matsuda, *Nano Res.* **10**, 546 (2017).
- [10] A. S. Sarkar and E. Stratakis, *Adv. Sci.* **7**, 2001655 (2020).
- [11] F. Li, X. Liu, Y. Wang, and Y. Li, *J. Mater. Chem. C* **4**, 2155 (2016).
- [12] S. Yu, H. D. Xiong, K. Eshun, H. Yuan, and Q. Li, *Appl. Surf. Sci.* **325**, 27 (2015).
- [13] L. C. Gomes, P. E. Trevisanutto, A. Carvalho, A. S. Rodin, and A. H. Castro Neto, *Phys. Rev. B* **94**, 155428 (2016).
- [14] Y.-H. Chan, D. Y. Qiu, F. H. da Jornada, and S. G. Louie, *Proc. Natl. Acad. Sci. (USA)* **118**, e1906938118 (2021).
- [15] L. Xu, M. Yang, S. J. Wang, and Y. P. Feng, *Phys. Rev. B* **95**, 235434 (2017).
- [16] V. K. Dien, O. K. Le, V. Chihaiia, M.-P. Pham-Ho, and D. N. Son, *J. Comput. Electron.* **20**, 135 (2021).
- [17] V. K. Dien, N. T. Han, W. Bang-Li, K. Lin, and M. Lin, *Adv. Theory Simul.* **6**, 2200950 (2023).
- [18] N. T. T. Tran, D. K. Nguyen, O. E. Glukhova, and M.-F. Lin, *Sci. Rep.* **7**, 17858 (2017).
- [19] V. K. Dien, W.-B. Li, K.-I. Lin, N. T. Han, and M.-F. Lin, *RSC Adv.* **12**, 34851 (2022).
- [20] H.-C. Chung, C.-P. Chang, C.-Y. Lin, and M.-F. Lin, *Phys. Chem. Chem. Phys.* **18**, 7573 (2016).
- [21] W. Zhou, X. Zou, S. Najmaei, Z. Liu, Y. Shi, J. Kong, J. Lou, P. M. Ajayan, B. I. Yakobson, and J.-C. Idrobo, *Nano Lett.* **13**, 2615 (2013).
- [22] P. K. Chow, R. B. Jacobs-Gedrim, J. Gao, T.-M. Lu, B. Yu, H. Terrones, and N. Koratkar, *ACS Nano* **9**, 1520 (2015).
- [23] V. Van On, P. T. Bich Thao, L. N. Thanh, and N. T. Tien, *AIP Adv.* **12**, 095318 (2022).
- [24] Y. Li, T. Wang, M. Wu, T. Cao, Y. Chen, R. Sankar, R. K. Ulaganathan, F. Chou, C. Wetzel, and C.-Y. Xu, *2D Mater.* **5**, 021002 (2018).
- [25] I. M. Datye, A. Daus, R. W. Grady, K. Brenner, S. Vaziri, and E. Pop, *Nano Lett.* **22**, 8052 (2022).
- [26] J.-H. Wong, B.-R. Wu, and M.-F. Lin, *J. Phys. Chem. C* **116**, 8271 (2012).
- [27] R. G. Parr, *Annu. Rev. Phys. Chem.* **34**, 631 (1983).
- [28] A. Pecchia, G. Penazzi, L. Salvucci, and A. Di Carlo, *New J. Phys.* **10**, 065022 (2008).
- [29] D. Wing, J. B. Haber, R. Noff, B. Barker, D. A. Egger, A. Ramasubramaniam, S. G. Louie, J. B. Neaton, and L. Kronik, *Phys. Rev. Mater.* **3**, 064603 (2019).
- [30] J. Hafner, *J. Comput. Chem.* **29**, 2044 (2008).
- [31] S. Smidstrup, T. Markussen, P. Vancraeyveld, J. Wellendorff, J. Schneider, T. Gunst, B. Verstichel, D. Stradi, P. A. Khomyakov, and U. G. Vej-Hansen, *J. Phys.: Condens. Matter* **32**, 015901 (2020).
- [32] J. P. Perdew, K. Burke, and M. Ernzerhof, *Phys. Rev. Lett.* **77**, 3865 (1996).
- [33] G. Kresse and D. Joubert, *Phys. Rev. B* **59**, 1758 (1999).
- [34] P. Wisesa, K. A. McGill, and T. Mueller, *Phys. Rev. B* **93**, 155109 (2016).
- [35] M. Shishkin and G. Kresse, *Phys. Rev. B* **74**, 035101 (2006).
- [36] See Supplemental Material at <http://link.aps.org/supplemental/10.1103/PhysRevB.108.205406> for in-depth information on the structural stability of strained GeS monolayers, details on the coverage test, additional data regarding the electronic and optical properties of GeS monolayers, as well as insights into the selection role in anisotropic optical responses. The Supplemental Material also contains Refs. [63–66].
- [37] M. Rohlfing and S. G. Louie, *Phys. Rev. B* **62**, 4927 (2000).
- [38] N. T. Kaner, Y. Wei, Y. Jiang, W. Li, X. Xu, K. Pang, X. Li, J. Yang, Y. Jiang, and G. Zhang, *ACS Omega* **5**, 17207 (2020).
- [39] Y. Xu, K. Xu, and H. Zhang, *Molecules* **24**, 639 (2019).
- [40] T. Hu and J. Dong, *Phys. Chem. Chem. Phys.* **18**, 32514 (2016).
- [41] K. D. Pham, C. V. Nguyen, H. V. Phuc, T. V. Vu, N. V. Hieu, B. D. Hoi, L. C. Nhan, V. Q. Nha, and N. N. Hieu, *Superlattices Microstruct.* **120**, 501 (2018).
- [42] W. Zachariasen, *Phys. Rev.* **40**, 917 (1932).
- [43] G. Pizzi, V. Vitale, R. Arita, S. Blügel, F. Freimuth, G. Géranton, M. Gibertini, D. Gresch, C. Johnson, T. Koretsune *et al.*, *J. Phys.: Condens. Matter* **32**, 165902 (2020).
- [44] W. Ku and A. G. Eguluz, *Phys. Rev. Lett.* **89**, 126401 (2002).
- [45] J. Bardeen and W. Shockley, *Phys. Rev.* **80**, 72 (1950).
- [46] S. Bruzzone and G. Fiori, *Appl. Phys. Lett.* **99**, 222108 (2011).
- [47] M. Cheng and J. Guan, *Phys. Rev. Mater.* **5**, 054005 (2021).
- [48] R. Fei and L. Yang, *Nano Lett.* **14**, 2884 (2014).
- [49] G. Guo and G. Bi, *Micro Nano Lett.* **13**, 600 (2018).
- [50] E. G. Emberly and G. Kirczenow, *Phys. Rev. B* **61**, 5740 (2000).
- [51] Y. Ding, Y.-S. Liu, G. Yang, Y. Gu, Q. Fan, N. Lu, H. Zhao, Y. Yu, X. Zhang, X. Huo *et al.*, *ACS Appl. Electron. Mater.* **3**, 1151 (2021).
- [52] D. Y. Qiu, F. H. da Jornada, and S. G. Louie, *Phys. Rev. B* **93**, 235435 (2016).
- [53] W.-H. Li, J.-D. Lin, P.-Y. Lo, G.-H. Peng, C.-Y. Hei, S.-Y. Chen, and S.-J. Cheng, *Nanomaterials* **13**, 1739 (2023).

- [54] D. Y. Qiu, F. H. da Jornada, and S. G. Louie, *Phys. Rev. Lett.* **111**, 216805 (2013).
- [55] L. Yang, J. Deslippe, C.-H. Park, M. L. Cohen, and S. G. Louie, *Phys. Rev. Lett.* **103**, 186802 (2009).
- [56] C. Robert, D. Lagarde, F. Cadiz, G. Wang, B. Lassagne, T. Amand, A. Balocchi, P. Renucci, S. Tongay, B. Urbaszek, and X. Marie, *Phys. Rev. B* **93**, 205423 (2016).
- [57] G.-H. Peng, P.-Y. Lo, W.-H. Li, Y.-C. Huang, Y.-H. Chen, C.-H. Lee, C.-K. Yang, and S.-J. Cheng, *Nano Lett.* **19**, 2299 (2019).
- [58] M. Palummo, M. Bernardi, and J. C. Grossman, *Nano Lett.* **15**, 2794 (2015).
- [59] N. Sanders, D. Bayerl, G. Shi, K. A. Mengle, and E. Kioupakis, *Nano Lett.* **17**, 7345 (2017).
- [60] M. Re Fiorentin, F. Risplendi, M. Palummo, and G. Cicero, *ACS Appl. Nano Mater.* **4**, 1985 (2021).
- [61] Y. Chen and S. Y. Quek, *2D Mater.* **5**, 045031 (2018).
- [62] H. Shi, R. Yan, S. Bertolazzi, J. Brivio, B. Gao, A. Kis, D. Jena, H. G. Xing, and L. Huang, *ACS Nano* **7**, 1072 (2013).
- [63] B. Sa, Y.-L. Li, J. Qi, R. Ahuja, and Z. Sun, *J. Phys. Chem. C* **118**, 26560 (2014).
- [64] M. Manju, S. Thomas, P. Anees, S. U. Lee, and K. Ajith, *J. Ind. Eng. Chem.* **90**, 399 (2020).
- [65] M. Fox, *Optical Properties of Solids*, Oxford Master Series in Physics Vol. 3 (Oxford University Press, Oxford, England, 2002).
- [66] A. Togo, *J. Phys. Soc. Jpn.* **92**, 012001 (2023).